Symmetry-Broken Charge-Transfer Excited State in Homoleptic Zinc(II) Imidazo[1,2- a]pyridine Complexes

Valerio Giuso, Elise Jouaiti, Cristina Cebrián, Sabrina Parant-Aury, Nathalie Kyritsakas, Christophe Gourlaouen, Matteo Mauro

ChemPhotoChem

Research Articles
doi.org/10.1002/cptc.202300092

Chemistry Europe
European Chemical Societies Publishing

www.chemphotochem.org

Special Collection

Symmetry-Broken Charge-Transfer Excited State in Homoleptic Zinc(II) Imidazo[1,2-*a*]pyridine Complexes

Valerio Giuso,[a] Elise Jouaiti,[a] Cristina Cebrián,[b] Sabrina Parant-Aury,[c] Nathalie Kyritsakas,[d] Christophe Gourlaouen,[e] and Matteo Mauro*[a]

A series of four homoleptic cationic Zn^{II} complexes (**Zn1**–**Zn4**) coordinated by two substituted *bis*-imidazo[1,2-*a*]pyridine (ImPy) ligands (**L1**–**L4**) is herein presented. The ligands are functionalized with either electron acceptor or donor functional groups at the C6 positions of the two ImPy moieties. In DMF solution, all of the complexes display intense near-UV to blue emission (λ_{em} = 379–450 nm) with high photoluminescence quantum yields (PLQY) up to 0.50 and short-lived excited states. Additionally, complex **Zn4**, containing the -NPh_2 functionalized ligand, displays an interesting solvatochromic behavior. The absorption spectrum is characterized by electronic transitions with mainly ligand-centered (^{1}LC) and intraligand charge-transfer (^{1}ILCT) character, which involves a symmetric electron density redistribution at Franck-Condon (FC). In stark contrast, the subsequent excited-state dynamics relaxes the molecular symmetry and allows symmetry-breaking hole-electron pair redistribution on the bichromophoric system. As a consequence, an efficient radiative de-excitation process takes place that is ascribed to a singlet-manifold excited state with symmetry-broken charge transfer (^{1}SBCT) character, as supported by an in-depth photophysical, electrochemical and time-dependent density functional theory (TD-DFT) investigation. Remarkably, the ^{1}SBCT nature provides structureless green photoluminescence in the solid state (λ_{em} up to 520 nm for **Zn4**), which is rather uncommon for Zn^{II} complexes.

Introduction

Light-promoted symmetry-breaking charge transfer (SBCT) is a fundamental process occurring in natural light-harvesting systems. In the bacterial photosynthetic reaction center, photo-induced ultrafast charge separation (CS) takes place from a virtually symmetric light-harvesting complex and yields an asymmetric electron transfer (ET) cascade process.[1–4] The chemical engineering of Nature-inspired systems that mimic biological photoinduced SBCT processes is of great interest not only from fundamental point of view, but also because such chromophoric systems find potential applications in artificial photosynthesis and organic-photovoltaics (OPV) with facilitated CT exciton formation and separation.[5–7] Yet, it is a rather challenging task.

9,9′-Bianthryl derivatives are by far the most investigated compounds that display SBCT, where the nearly orthogonal arrangement of the two chromophores ensures weak electronic coupling between the two fused-aromatic moieties and enables radiative recombination back to the electron ground state (GS) from a symmetry-broken intramolecular charge transfer (ICT) manifold.[8–10]

In this framework, organometallic compounds bearing main-group elements[11–12] as well as transition metals,[13–15] have attracted much attention as well. For instance, in the well-known and archetypal orange-red triplet emitter [Ru(2,2′-bipyridine)$_3$]$^{2+}$ the emissive triplet metal-to-ligand charge transfer (^{3}MLCT) state is thought to localize onto one of the three virtually identical 2,2′-bipyridine ligands, hence to display symmetry-broken character,[16–18] although this is still debated.

Homoleptic Zn^{II} dipyrromethene complexes are highly absorbing bichromophoric systems that feature two identical dipyrrins adopting a virtually orthogonal geometry at their ground state. In such compounds, radiative de-excitation takes place in non-polar solvents with moderate to good efficiency, whereas population of a poorly emissive SBCT state occurs in

[a] *V. Giuso, E. Jouaiti, Dr. M. Mauro*
Institut de Physique et Chimie des Matériaux de Strasbourg, UMR7504
Université de Strasbourg, CNRS
23 rue du Loess, 67034 Strasbourg (France)
E-mail: mauro@unistra.fr
[b] *Dr. C. Cebrián*
Laboratoire Lorraine de Chimie Moléculaire (L2CM)
Institut de Chimie, Physique et Matériaux (ICPM)
Université de Lorraine, CNRS
1 Boulevard François Arago, 57078 Metz (France)
[c] *Dr. S. Parant-Aury*
Laboratoire Lorraine de Chimie Moléculaire (L2CM)
Université de Lorraine, CNRS
Blvd. des Aiguillettes, 54506 Nancy (France)
[d] *N. Kyritsakas*
Service de Radiocristallographie
Fédération de chimie Le Bel – FR2010
BP 296R8
1, rue Blaise Pascal, 67008 Strasbourg (France)
[e] *Dr. C. Gourlaouen*
Laboratoire de Chimie Quantique
Institut de Chimie de Strasbourg UMR7177
Université de Strasbourg-CNRS
4 Rue Blaise Pascal, 67008 Strasbourg (France)

Supporting information for this article is available on the WWW under https://doi.org/10.1002/cptc.202300092

An invited contribution to a Special Collection celebrating the 5 Year Anniversary of *ChemPhotoChem*

weak to highly polar solvents.[13–15,19–20] More recently, Herbert, Williams and co-workers reported on an interesting family of homoleptic, hexacoordinated Zn^{II} complexes displaying intense yellow emission from a triplet-manifold with SBCT character, namely ^{3}SBCT.[21]

Highly-emissive compounds based on first-row earth-abundant metals are appealing nowadays as they are potential candidates for replacing emitters with rarer, more expensive and toxic Ir^{III} and Pt^{II} complexes.[22–29] These latter are by far leading emitters in the field of light-emitting devices currently due to their outstanding redox and optical properties. Alternatively, Cu^{I}[30–38] and Zn^{II}[39–40] complexes are attracting growing interest owing to their d^{10} electronic configuration that rules out the possibility of populating low-lying metal-centered (MC) quenching states.

Tetradentate Schiff base ligands,[39,41] bidentate 7-azaindoles,[42] pyridyl-1,2,4-triazole,[43] pyridyl-phenanthro[9,10-*d*]imidazole,[44] imidazo[1,2-*a*]pyridines,[45] and imidazo[1,5-*a*]pyridines,[46–49] were previously investigated for the formation of luminescent Zn^{II} complexes and typically displayed ligand-centered emission. A few examples of Zn^{II} derivatives displaying thermally-activated delayed emission (TADF) process are also known.[50–52]

Aiming at designing efficient emitters based on earth-abundant metals, we herein disclose a novel family of homoleptic *bis*-tridentate Zn^{II} complexes of general formula $[Zn(L)_2](BF_4)_2$, where L is a substituted 2,6-*bis*(imidazo[1,2-*a*]pyridin-2-yl)pyridine ligand. This latter is symmetrically functionalized with either electron acceptor or donor groups at the C6 positions, providing chromophoric systems with NNN coordination sites that are readily prone to coordinate a Zn^{II} ion. The resulting four complexes display appealing optical properties with emission in the near-UV to blue, which for some arises from a SBCT exited state as jointly supported by photophysical, electrochemical and computational investigation.

Results and Discussion

Synthesis and X-ray structural analysis

The synthesis and the structural characterization of the ligand **L1**–**L4** was previously described by us (see Scheme S1 of the Supplementary Information for chemical structures).[53] The homoleptic Zn^{II} complexes $[Zn(\mathbf{L1}–\mathbf{L4})_2](BF_4)_2$, namely **Zn1**–**Zn4**, were prepared straightforwardly by reacting the corresponding ligand **L1**–**L2** with $Zn(BF_4)_2$ as the Zn^{II} source in a 2:1 molar ratio in a 1:1 solvent mixture of $CHCl_3$:MeOH under reflux. The compounds were obtained as white to off-white microcrystalline solids and have fair to good solubility in polar organic solvents. Their chemical structure is displayed in Scheme 1. The desired complexes were fully characterized by means of ^{1}H, ^{13}C{^{1}H} and ^{19}F{^{1}H} NMR (when applicable) spectroscopy and high-resolution electrospray ionization mass spectrometry (HR-ESI-MS). The corresponding spectra are displayed in Figure S1–S9 of the Supporting Information.

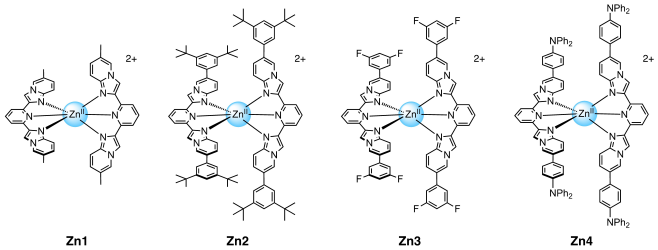

Scheme 1. Chemical structure of the four homoleptic Zn^{II} complexes (**Zn1**–**Zn4**) investigated. All the complexes were prepared as BF_4^- salts.

Single crystals of compound **Zn2** of quality suitable for X-ray diffractometric analysis were grown in acetone solution by vapor diffusion of Et_2O. The corresponding ORTEP diagram is displayed in Figure 1. Their structural characterization helped to unambiguously confirm their atom connectivity and crystalline arrangement. In this condition, complex **Zn2** crystalizes in the centrosymmetric *P*-1 space group solvated with one acetone molecule. The Zn^{II} ion adopts an octahedral geometry distorted in order to comply with the constraints imposed by the two tridentate 2,6-bis(6-(3,5-di-*tert*-butylphenyl)imidazo[1,2-*a*]pyridin-2-yl)pyridine ligands and with two pyridine of the mutual *trans* position. In particular, the Zn–N bond distances lie between 2.130(3) and 2.169(3) Å and the bond angle N(1)–Zn–N(5) and N(6)–Zn–N(10) are 150.7° and 150.0°, respectively. The two tridentate ligands adopt a nearly orthogonal arrangement with N_{ImPy1}–Zn–N_{ImPy2} close to 90°.

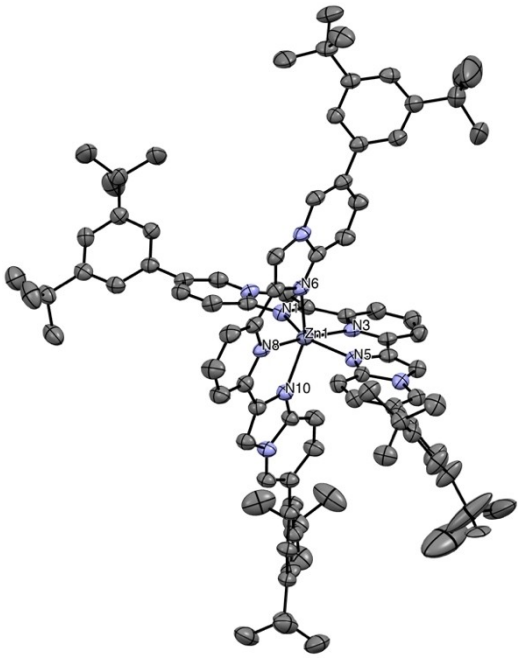

Figure 1. ORTEP diagram of the molecular structure of complex **Zn2**, as determined by single-crystal X-ray diffraction, with a partial labeling scheme. Anisotropic displacement ellipsoids are drawn at the 50% level of probability. Hydrogen atoms, BF_4^- counterions and acetone solvent molecule are omitted for clarity.

Table 1. Photophysical data recorded for samples of compounds **Zn1**–**Zn4** in DMF solution at concentration of 3.0×10^{-6} M at room temperature and in 2-MeTHF glassy matrix at 77 K.

Compound	λ_{abs} [nm] (ε [10^4 $M^{-1}cm^{-1}$])	λ_{em} [nm]	PLQY	τ [ns]	k_r [10^6 s^{-1}][a]	k_{nr} [10^6 s^{-1}][a]	λ_{em} [nm]	τ [ns]
	room temperature							*77 K*
Zn1	319*sh* (3.73) 332 (4.33) 345*sh* (3.37)	363*sh*, 379, 400*sh*	0.28	4.46	62.7	0.16	352, 370, 390, 411*sh*	1.17 (51 %) 2.89 (49 %)
Zn2	331 (4.37) 352*sh* (2.37)	392	0.26	3.87	67.1	0.19	368, 387, 409*sh*	1.51 (31 %) 7.28 (23 %) 3.29 (46 %)
Zn3	329 (2.83)	412	0.18	5.11	35.2	0.16	369, 388, 408	1.65 (34 %) 6.39 (66 %)
Zn4	309 (12.63) 341 (13.97)	450	0.50	4.28	116	0.12	437	1.77 (62 %) 4.42 (38 %)

[a] k_r and k_{nr} were estimated by using the following equations $k_r = PLQY/\tau$ and $k_{nr} = (1 - PLQY)/\tau$; *sh* denotes a shoulder.

Photophysical properties

For the four novel complexes **Zn1**–**Zn4**, the photophysical data recorded in dilute DMF solution (concentration $= 3.0\times10^{-6}$ M) at room temperature are listed in Table 1 and the corresponding UV-Vis absorption and photoluminescence spectra are displayed in Figure 2, along with the spectra recorded in 2-MeTHF glassy matrix at 77 K. Compounds **Zn1**–**Zn3** display similar absorption profiles in the region $\lambda_{abs} = 300$–370 nm that are characterized by two partially overlapping bands. As far as complex **Zn1** is concerned, its UV-vis absorption spectrum shows an intense ($\varepsilon = 4.3\times10^4$ $M^{-1}cm^{-1}$) band peaking at 332 nm. A second maximum at 345 nm is also present with lower intensity ($\varepsilon = 3.4\times10^4$ $M^{-1}cm^{-1}$). Both absorption processes are attributable to electronic transitions with admixed singlet-manifold ligand-centered (^{1}LC) and intraligand charge-transfer (^{1}ILCT) character involving the coordinated tridentate ligands. The absorption onset displays a small bathochromic shift when going from compound **Zn1** to **Zn2** to **Zn3**. Overall, these findings indicate that the direction of the charge-transfer vector and the variation of the energetic gap of the π-π^* transition located onto the ligands compensate each other when comparing **Zn2** to **Zn3** derivative that feature substituents (*i.e.* fluorine *vs* tert-butyl) with opposite electronic effect.

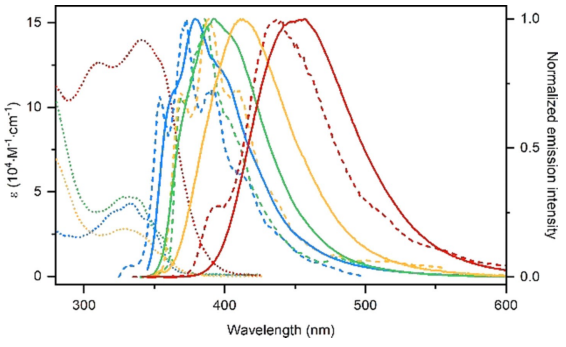

Figure 2. Electronic UV-vis absorption (dotted traces) and emission (solid traces) spectra of complexes **Zn1** (blue traces), **Zn2** (green traces), **Zn3** (orange traces) and **Zn4** (red traces) in air-equilibrated DMF solution at concentration of 3×10^{-6} M at room temperature. Low temperature emission spectra in 2-MeTHF glassy matrix are displayed as dashed traces. The samples were excited at $\lambda_{exc} = 320$ nm.

Compound **Zn4** displays a much more intense absorption spectrum with two better resolved maxima at $\lambda_{abs} = 309$ and 341 nm, being $\varepsilon = 1.26\times10^5$ and 1.4×10^5 $M^{-1}cm^{-1}$, respectively, and absorption onset extending towards the visible region. In all cases, absorption spectra are reminiscent of the free proligands[53] apart from the obvious nearly doubled extinction coefficients recorded for the Zn^{II} complexes. Weak to negligible dipolar coupling is observed as expected due to the nearly orthogonal arrangement of the two chromophoric ligands.

Upon photoexcitation in the lower-energy band at $\lambda_{exc} =$ 300–350 nm, all the samples display near-UV to blue emission in diluted DMF with maximum at 379 (**Zn1**), 392 (**Zn2**), 412 (**Zn3**) and 450 (**Zn4**) nm with good to high photoluminescence quantum yield (PLQY) in the range 0.18–0.50. The highest PLQY value is recorded for derivative **Zn4** bearing four triphenylamine pendant groups. Interesting, moving along the series from **Zn1** to **Zn4** a loss of structural feature is clearly visible in the emission profile. This effect is accompanied by an increase of the Stokes shift and broadening of the spectral profile, which is indicative of the enhancement of the charge transfer (CT) character of the emitting state along the series, as also confirmed by the hypsochromic shift observed upon lowering the temperature down to 77 K (Figure 2 and Table 1). Excited state lifetimes fall in the few ns time scale with values in the order of 3.9–5.1 ns in solution, which corresponds to radiative rate constant, k_r, values as high as 3.5–11.2×10^7 s^{-1} and strongly supporting the fluorescence nature of the radiative process.

The solvatochromic properties were investigated for complex **Zn4** by measuring its photophysical features in solvents of various polarities. The solvent-dependent absorption and emission spectra are displayed in Figures S12–S13 and the corresponding data are compiled in Table S3 of the Supporting Information. Negligible solvent effect was observed for derivative **Zn2** instead (data not shown).

As far as complex **Zn4** is concerned, the absorption profile appeared to be only slightly influenced by the solvent polarity. On the other hand, the maximum of the emission wavelength was affected to a much larger extent showing a bathochromic shift upon increasing polarity. This effect suggests that environmental effects mainly concern the solvent stabilization of the

emissive excited state and that a sizeable increase of the CT character from Franck-Condon (FC) to relaxed state takes place. The positive solvatochromism observed in the emission spectra gives rise to a sizeable shift of the emission maximum from 407 to 462 nm when going from the least polar 1,4-dioxane to the most polar DMSO. Noteworthy, such spectral change is accompanied by a slight prolongation of the excited-state lifetime (1.88 *vs* 4.89 ns, respectively) and by a remarkable enhancement of the PLQY from 0.20 to 0.59. A closer look at the de-excitation kinetic constants is instructive, since it reveals that solvent effect influences mainly k_{nr}, whereas k_r values remain comparable upon changing solvent polarity (Table S3). This is indicative of a similar character of the radiative process observed in different solvents and that solvation affects radiationless channels only.

To gain deeper insights into the character of the lowest-lying electronic absorption and emission states involved into the optical processes, Stokes shift was plotted against the solvent orientation polarizability following the Lippert–Mataga relationship [Equation (1)]:[54–55]

$$\Delta\bar{\nu} = \bar{\nu}_{abs} - \bar{\nu}_{em} = \frac{2(\mu_e - \mu_g)^2}{hca^3}\left(\frac{\varepsilon_0 - 1}{2\varepsilon_0 + 1} - \frac{n^2 - 1}{2n^2 + 1}\right) + b \qquad (1)$$

where $\bar{\nu}_{abs}$ and $\bar{\nu}_{em}$ are the absorption and emission maximum, respectively, given in wavenumbers, $(\mu_e - \mu_g)$ is the difference between the excited (μ_e) and ground μ_g state dipole moment, respectively, *a* is the Onsager radius, *h* is the Planck's constant, *c* is the speed of light, the solvent-specific ε_0 and *n* are the local relative permittivity and refractive index, respectively, and *b* is the observed emission in the absence of environment-dependent processes. The term Δf defined as by Equation (2) is called solvent orientation polarizability.

$$\Delta f = \frac{\varepsilon_0 - 1}{2\varepsilon_0 + 1} - \frac{n^2 - 1}{2n^2 + 1} \qquad (2)$$

Additionally, observed solvent-dependent Stokes shift was plotted as a function of the sole relative permittivity component following Equation (3):

$$\Delta\bar{\nu} = \frac{2(\mu_e - \mu_g)^2}{hca^3}\left(\frac{\varepsilon_0 - 1}{2\varepsilon_0 + 1}\right) + b' \qquad (3)$$

Both plots are displayed in Figure S14 and show a linear relationship with slope of the regression of *ca.* 8300 and 9300 following eqn. 1 and 3, respectively, which indicate that the observed solvatochromic properties are mainly influenced by the environment dielectric constant, whereas the refractive index of the medium influences the solvatochromism to a lesser extent. Furthermore, these findings clearly confirm that compound **Zn4** is characterized by a large change of the dipole moment between the ground (and Franck-Condon) and emissive excited state, with little polar GS and highly polar emissive excited state. This latter can be tentatively described as having mainly ^{1}CT nature with $\pi_{Ph3N} \rightarrow {}^*\pi_{Pylm}$ character involving the electron-donor triarylamine (Ph_3N) and the electron-acceptor Pylm moieties (see computational section for further discussion).

Solid state samples of all the complexes display moderate, broad, and featureless photoluminescence that is bathochromically shifted compared to that observed in DMF solution, although an overall decrease of the PLQY is observed (see Figure S15 and Table S4 of the Supporting Information). Additionally, derivative **Zn2** undergoes an irradiation-time dependent decomposition that is slowly observed with the steady increase of a broad band at longer wavelengths (see Figure S16). The radiative process can be described with confidence as arising from an excited state with mainly ^{1}CT character. Noteworthy, solid-state samples of **Zn4** display green emission with maximum centered at $\lambda_{em} = 520$ nm, with a shift as large as *ca.* 3000 cm^{-1} compared to the sample in DMF solution. At this stage, it should be noticed that emission in the longer wavelength region of the electromagnetic spectrum, namely green to red, is rare for Zn^{II} complexes.

Computational investigation

Firstly, the structure of the four complexes **Zn1**–**Zn4** was optimized at its electronic GS in DMF as the solvent. The main geometrical data are summarized in Table S5 of the Supporting information. The computed structure reproduces well the experimental structural parameters obtained by X-ray diffraction for compound **Zn2**.

Starting from the optimized GS structures, absorption spectra were computed in DMF by means of time-dependent density-functional theory (TD-DFT) and the results are shown in Figure 3. Computed spectra are in very good agreement with experimental UV-Vis data (*cf.* Figure 2 and Figure 3) for derivatives **Zn1**–**Zn3**, whereas the computation overestimates the absorption at longer wavelengths for derivative **Zn4**. The computed transitions, along with their energy and oscillator strength, are listed in Table S6–S7 of the Supporting Information. All complexes present an electronic absorption band around 330–350 nm that is the result of the combination of several energetically close electronic transitions with singlet character, namely S_1, S_2, S_3 and S_4 for **Zn1**, as an example (see

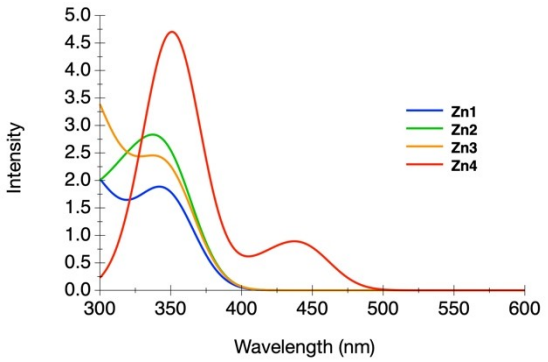

Figure 3. Electronic UV-Vis absorption spectra for the different Zn(II) complexes **Zn1**–**Zn4** computed in DMF by means of TD-DFT.

Table S6). As far as complex **Zn1** is concerned, all the computed transitions share a similar nature, which can be described as charge transfer (CT) with $\pi_{ImPy} \rightarrow {}^*\pi_{py}$ character from the lateral imidazopyridine fragments towards the central pyridine moiety as depicted in the electron density difference map shown in Figure 4. This excitation process involves both tridentate chromophoric ligands with a spherically symmetric and delocalized redistribution of the electron-hole pair density. Similar attribution can be made for the transition computed in the spectral region at 330–350 nm for derivatives **Zn2**–**Zn4**. Thus, this picture agrees well with the experimental findings (see photophysical section).

A difference between the computed and experimental spectrum appears in the visible region for derivative **Zn4**. In the computed spectrum, an absorption band centered at 466 nm is present due to a series of electronic transitions with symmetrical CT character involving an electron displacement from the Ph_2NPh– fragments towards the central *bis*-ImPy moiety of the ligand (Figure 5). This apparent difference can be due to the coexistence of several conformers in solution in equilibrium at room temperature that are expected to yield different absorption bands. On the other hand, only the electronic processes arising from the most stable conformer have been computed for sake of calculation.

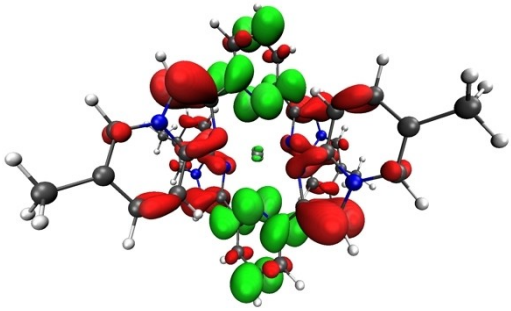

Figure 4. Electron density difference map between the ground and S_1 excited state of complex **Zn1** at the Franck-Condon geometry. Electronically depleted and enriched areas are in red and in green colors, respectively.

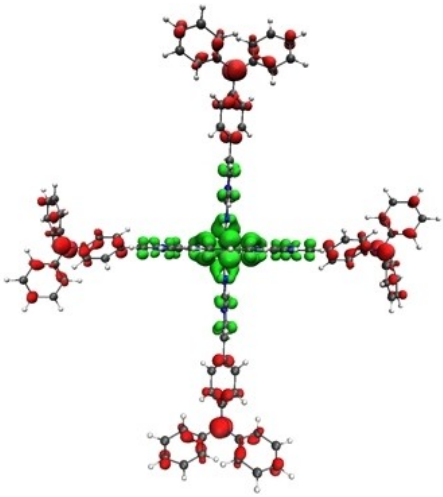

Figure 5. Electron density difference map between the ground and S_1 excited state of complex **Zn4** at the Franck-Condon geometry. Electronically depleted and enriched areas are in red and in green colors, respectively.

Expectantly, no transition with direct involvement of the Zn^{II} center could be identified in the spectra due to the mainly electrostatic nature of the metal-ligand interaction in such kind of complexes, which also confirms that Zn^{II} ion acts mainly as a relatively innocent bridge between the two orthogonally-oriented chromophores. Nevertheless, the coordination of the ligand **L1**–**L4** on the Zn^{II} cation induces some electronic perturbation with significant spectral changes of the former in terms of both energetics and transition character when compared to the free pro-ligand. In complex **Zn1** the lowest-energy main absorption band shifts bathochromically compared to the free ligand **L1**, the computed wavelength being at 349 nm *vs.* 325 nm for the former and the latter, respectively.[53] This shift is accompanied by a change of the character of the transition that becomes almost pure ^{1}ILCT in **Zn1**, whereas it has a mixed ^{1}LC/^{1}ILCT nature in free **L1**. A similar spectral and nature change is found for derivative **Zn2**.

An even more pronounced difference is found for **Zn3** when compared to the free pro-ligand **L3**. For the former, the character of the S_1 transition becomes similar to that computed for derivative **Zn1**–**Zn2** with electron density displacement occurring from lateral ImPy fragments towards the pyridine moiety. The pyridine ring becomes a better electron π-acceptor compared to the difluorophenyl fragment upon coordination to the divalent Zn^{II} ion. No involvement of the difluorophenyl moiety is observed. For proligand **L3**, it was found to have an ILCT character from the pyridine/imidazopyridine towards the peripheral difluorophenyl fragments.

In stark contrast, the nature of the S_1 transition remains rather similar between free **L4** and **Zn4** and it can be described as a spherically-symmetric ILCT from the electron-rich Ph_2NPh– fragment towards the ImPy core of the ligand. The symmetric redistribution of the electron density agrees well with the weak solvatochromism observed in the absorption spectra (see Figure S12–14 and Table S3 of the Supporting Information).

To gain deeper insights into the nature and character of the emission processes the lowest-lying emissive single-manifold excited state was then optimized for all the investigated complexes. Given the D_2 point group symmetry of the GS structure, excited-state optimization was performed retaining the D_2 symmetry constrain at the first stage. Geometrical and energetic parameters are listed in Table 2 for **Zn1**. Table S8–S10 summarizes the corresponding data for derivatives **Zn2**–**Zn4**. For selected atom numbering see Scheme S2 of the Supporting Information.

As far as **Zn1** is concerned, the D_2-optimized structure (called S_{1C} hereafter) shows minor geometrical distortions compared to the corresponding computed GS structure. The structure displays only a slight contraction of the Zn–N^1 and Zn–$N^{1\prime}$ bond distances and a small lengthening of the Zn–N^2, Zn–$N^{2\prime}$, Zn–N^3 and Zn–$N^{3\prime}$ distances for all the complexes. Obviously, under such symmetry constrain, the two ligands are forced to be virtually identical (Figure 6), and the resulting S_1 excitation is delocalized over the two ligands as observed at Franck-Condon geometry (Figure 4).

Table 2. Selected geometrical and energetic parameters computed for the different energy minima for complex **Zn1** optimized under different point group symmetry constrains. Distances and angles are given in Å and [°], respectively. Energies differences are given in eV and compared to the computed lowest-lying singlet state. The associated emission wavelength computed for each structure is given in nm.

Parameter	GS	S_{1A} (C_1)	S_{1B} (C_2)	S_{1C} (D_2)
Zn–N^1	2.170	2.195	2.192	2.113
Zn–N^2	2.175	2.159	2.176	2.197
Zn–N^3	2.175	2.160	2.176	2.197
Zn–$N^{1\prime}$	2.170	2.071	2.056	2.113
Zn–$N^{2\prime}$	2.175	2.061	2.225	2.197
Zn–$N^{3\prime}$	2.175	2.583	2.225	2.197
N^1–Zn–$N^{1\prime}$	180.0	151.9	180.0	180.0
$N^{2\prime}$–$N^{1\prime}$–N^1–N^2	89.2	80.3	89.0	88.0
ΔE		0.000	0.006	0.099
λ_{em}		426	390	369

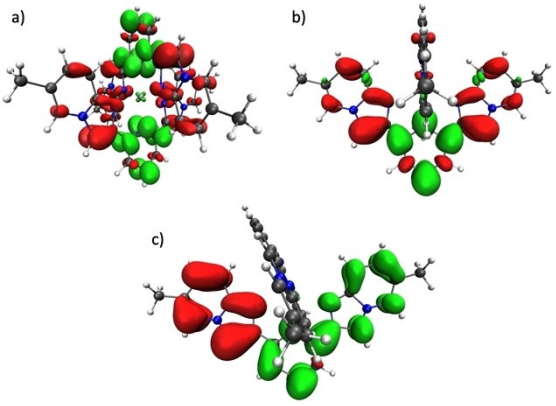

Figure 6. Electron density difference between the ground and S_1 excited state of complex **Zn1** at a) S_{1C} (D_2), b) S_{1B} (C_2), c) S_{1A} (C_1) optimized geometries. Electronically depleted and enriched areas are in red and in green colors, respectively.

Lowering the symmetry constrain to C_2 yields a different local minimum-energy geometry, namely S_{1B}, that is more stable by 93 meV compared to the D_2 structure and it results into major geometrical and electronic differences (see S_{1B} entry in Table 2). In the C_2-structure the excitation localizes on one of the two ligands with a consequent shortening (by *ca.* 0.1 Å) and elongation (by *ca.* 0.05 Å) of the Zn–$N^{1\prime}$ and Zn–$N^{2\prime}$/Zn–$N^{3\prime}$ bond distances, respectively. The ligand that is not involved into the excitation process remains relatively unchanged compared to the GS structure. The S_{1B} excited state can be described as having a singlet-manifold solvent-induced ^{1}SBCT character with a net electron density displacement from the two imidazopyridines moiety towards the central pyridine ring (Figure 6).

Relaxing the geometry of the S_1 state without symmetry constrain yields a minimum geometry (namely S_{1A}), lower by *ca.* 100 meV compared to the D_2 structure, characterized by an even deeper symmetry-broken geometry (see entry S_{1A} in Table 2 for selected geometrical parameters) with localization of the excited state on only one of the two coordinated ligands. Indeed, as shown in Figure 6 for compound **Zn1**, S_{1A} is characterized by an electron density displacement from one imidazopyridine to both the pyridine and the second imidazopyridine moiety. This ^{1}SBCT state gives rise to sizeable geometrical changes and desymmetrisation for the two Zn–N bonds involving the imidazopyridine moieties. Indeed, the S_{1A} structure displays large elongation of the Zn–$N^{3\prime}$ bond (d = 2.583 Å); whereas the Zn–$N^{2\prime}$ bond shortens to 2.061 Å. Moreover, large bending of the second ligand is observed as exemplified by the N^1–Zn–$N^{1\prime}$ angle of 151.9° in S_{1A} (compared to 180° in the GS). A similar picture can be drawn for complex **Zn2** and **Zn3**.

It should be noticed that S_{1A} state is characterized by a four-fold degeneracy onto the S_1 potential energy surface (PES). The pair of minimum localized on one ligand is separated by a very low energetic barrier that can be evaluated as energy difference with the C_2 symmetric S_{1B} structure (Figure S17). At this point it could be reasonable to hypothesize that fast hopping of the excitation between these degenerate states may take place on a time scale faster than solvation relaxation, but time-resolved ultrafast spectroscopical investigation would be needed to further elucidate such excited-state dynamics. Moreover, given the almost degenerate character of the S_{1A} and S_{1B} state both with ^{1}SBCT character, it is not possible at this stage to unambiguously assign the nature of the emitting state as being whether the former or the latter, although the emission wavelength computed for the C_2-symmetric S_{1B} state seems in better agreement with the experimental data, being λ_{em} = 390 nm (theoretical) vs 379 nm (experimental) for **Zn1** (cf. Table 1 and 2). This overall picture is similar for complexes **Zn2** and **Zn3** in agreement with the experimental findings that point towards a similar nature of the excited state for all the complexes. The corresponding geometrical and energetic data of the optimized structures are listed in Table S8 and S9 of the Supporting Information, respectively. Noteworthy, for derivative **Zn3** the S_{1C} state with D_2 symmetry lies as high as 249 and 247 meV higher in energy then the S_{1A} (C_1) and S_{1B} (C_2) states, respectively.

Overall, as could be seen in Table 2, Table S8 and Table S9, the computed energy difference between S_{1A} and S_{1B} states is very small for all complexes (< 50 meV) and comparable to thermal energy that account to 25 meV at 300 K. On the other hand, much higher energy differences (> 100 meV) are computed between S_{1C} and S_{1A}. The structures S_{1B} are probably much more representative to the average experimental structure, which explains the better agreement between the

emission wavelengths computed for the S_{1B} structures and the experimental ones.

The picture is somewhat different for complex **Zn4**. Optimization of S_1 within D_2 point group yields a delocalized excited state involving symmetrically both tridentate ligands (Figure 7 and S_{1C} in Table S10 of the Supporting Information), in agreement with what observed at the Franck-Condon geometry (see Figure 5) and corresponding to a doubly degenerated point on the S_1 PESs. As found for compound **Zn1**–**Zn3**, optimization within lower C_2 point group funnels S_1 into a structure of ^{1}SBCT character (S_{1B}, Figure 7) that is lower in energy by 39 meV compared to the S_{1C} structure and characterized by the localization of the excited state onto one of the two tridentate ligands. Full symmetry relaxation provides a minimum-energy state (S_{1A} with C_1 symmetry, see Table S10 and Figure 7 left) that lies 18 meV higher with highly localized excitation and with SBCT character involving electron density displacement from one of the four triarylamine groups to the pyridine-imidazopyridine fragment of the same ligand. This state is similar to the one found previously for the uncoordinated ligand **L4**.[53]

In addition, a second local minimum of C_1 symmetry (S_{1A1}) is found 56 meV above S_{1B} with ^{1}SBCT character where hole-electron pair is localized on two different ligands (Figure 7 and Table S10). As for the derivative **Zn1**, given the close energy between the S_{1A}, S_{1A1} and S_{1B} state computed for **Zn4** it is difficult to unambiguously assign the nature of the emitting state. Nevertheless, one can tentatively ascribe the observed emissive process as arising from the lowest-lying S_{1B} state, which would warrant better electronic coupling for the hole-electron pair and its faster radiative recombination to the ground state from the ^{1}SBCT state, in agreement with experimental photophysical and electrochemical findings (*vide infra*).

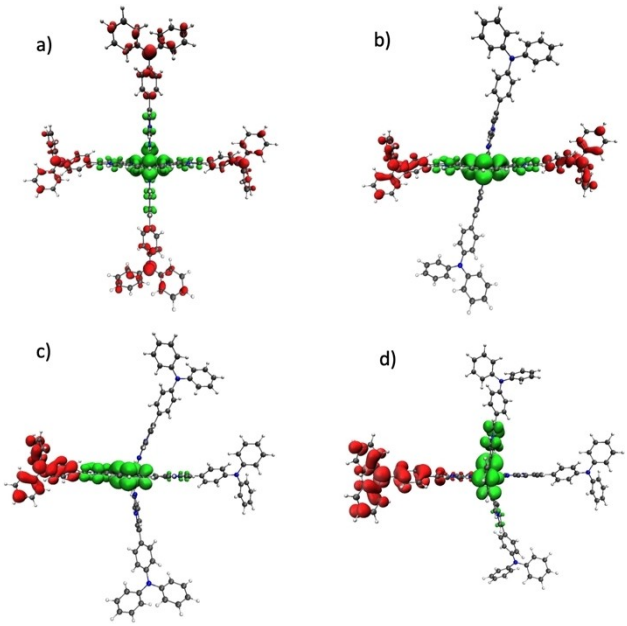

Figure 7. Electron density difference between the ground and the optimized geometries of the S_{1C} (a), S_{1B} (b), S_{1A} (c) and S_{1A1} (d) excited states computed for complex **Zn4**. Electronically depleted and enriched areas are in red and in green colors, respectively.

One last point is worth to mention concerns the computed structures for **Zn4**. As can be seen in Figure 7, the excited electron comes from the electron-rich triphenylamine fragment (red areas). Expectantly, there is large delocalization over the π system of three phenyl rings and the nitrogen lone pair and also with the imidazopyridine ring. In solution, rotation of aryl moieties about the C_{Ph}–N and C_{Ph}–C_{ImPy} axes is relatively free, reducing electronic overlap. The various rotamers are expected to be characterized by shifts of the absorption and emission spectral features compared to the ideally optimized theoretical structure and this effect may be accounted for the slightly different values between computed and experimental data of the emission. Such effect is already observed for other classes of chromophore with high rotational freedom.[56]

To further investigate the CT nature of the emitting excited state with ^{1}SBCT character, the energetics involved into the charge separation process was estimated to be exergonic by −1.01 and −0.85 eV for **Zn1** and **Zn4**, respectively, by using the simplified Weller equation [Equation (4)]:[57]

$$\Delta G_{CS} = e[E_{ox}(D) - E_{red}(A)] - E^* \quad (4)$$

where ΔG_{CS} is the driving force for charge separation, E_{ox}(D) and E_{red}(A) are the observed oxidation and reduction potential of the donor and acceptor moiety, respectively, measured by cyclic voltammetry in DMF (see Table S11 and Figure S18–S19 of the Supporting Information), e is the elemental charge, E^* is the energy of the excited state as estimated from the absorption maximum (see Table 1). The Coulombic interaction term E_c between the hole-electron pair has been neglected in the calculation.

Conclusion

In conclusion, a novel class of cationic Zn^{II} complexes is described featuring two substituted 2,6-*bis*(imidazo[1,2-*a*]pyridin-2-yl)pyridine ligands that are symmetrically functionalized with either electron acceptor or donor functional groups at the C6 positions of the two imidazo[1,2-*a*]pyridine moieties. The compounds display intense electronic absorption processes in the near-UV region that involve both tridentate chromophoric ligands with a spherically symmetric and delocalized redistribution of the electron-hole pair density. Upon photoexcitation, DMF samples displays short-lived photoluminescence in the near-UV to blue region with PLQY up to 0.50 that is ascribed to an emitting excited state with singlet-manifold ^{1}ICT character. For some of the derivatives, the emitting state can be better described as solvent-induced ^{1}SBCT with a net electron density displacement from the two imidazopyridines moiety towards the central pyridine ring involving only one of the two virtually identical tridentate ligands as supported by joint experimental and theoretical investigation. These results will help to shed better light onto the design of earth-abundant

metal complexes with optical and charge-transfer properties suitable for optoelectronic applications and light-harvesting systems.

Experimental Section

General considerations

Ligands **L1**–**L4** were prepared following our procedure described elsewhere.[53] $Zn(BF_4)_2$ was commercially available and used as received. Solvents and other commonly available reagents were purchased and used without further purification. Silica gel for column chromatography was purchased from Sigma-Aldrich. ^1H, $^{13}C\{^1H\}$ and $^{19}F\{^1H\}$ NMR spectra were recorded at 298 K on a Bruker AV500 spectrometer in deuterated solvents and the residual solvent peak was used as the internal reference. NMR spectra were calibrated to residual solvent signals. All the chemical shifts (δ) are reported in ppm. Mass spectrometry (HR-ESI-MS) was performed by the Service Spectrométrie de Masse of the Fédération de Chimie "Le Bel" FR2010 of the University of Strasbourg.

Synthesis of the complexes Zn1–Zn4

The tridentate ligand (**L1**–**L4**) was dissolved in chloroform (5 mL) under an argon atmosphere (**L1**: 0.1 g, 0.3 mmol; **L2**: 0.1 g, 0.14 mmol; **L3**: 0.1 g, 0.18 mmol; **L4**: 0.1 g, 0.12 mmol). Then, a solution containing 0.5 equiv. $Zn(BF_4)_2 \cdot 3H_2O$ (0.15 mmol, 0.07 mmol, 0.09 mmol and 0.06 mmol, respectively) in MeOH (5 mL) was added to the former solution and the resulting mixture was heated to reflux for 5 hours. After cooling down to room temperature, the half of volume volatiles was removed under vacuum and diethyl ether was added. The precipitate was filtered and washed three times with diethyl ether to give the target complex **Zn1**–**Zn4** as off-white solid.

Zn1: pro-ligand **L1** (0.1 g, 0.3 mmol), $Zn(BF_4)_2 \cdot 3H_2O$ (0.15 mmol), obtained 0.11 g, yield 77%. ^1H NMR (DMSO-d_6, 500 MHz): δ: 8.87 (s, 4H), 8.67 (t, $J=7.5$ Hz, 2H), 8.57 (d, $J=7.5$ Hz, 4H), 8.41 (s, 4H), 7.09 (d, $J=9$ Hz, 4H), 6.11 (d, $J=9$ Hz, 4H), 2.15 (s, 12H). $^{13}C\{^1H\}$ NMR (DMSO-d_6, 126 MHz) δ: 147.2, 142.6, 137.8, 133.3, 126.5, 124.5, 121.7, 113.3, 17.7. HR-MS (ESI): m/z $[M]^{2+}$ calcd for $C_{42}H_{35}N_{10}Zn$ 372.1124; found 372.1115.

Zn2: proligand **L2** (0.1 g, 0.14 mmol), $Zn(BF_4)_2 \cdot 3H_2O$ (0.07 mmol), obtained 0.08 g, yield 68%. ^1H NMR ($CDCl_3$, 500 MHz): δ: 8.81 (s, 4H), 8.62 (m, 6H), 8.43 (m, 4H), 7.45 (t, $J=1.7$ Hz, 4H), 7.43 (dd, $J=1.7$, 10 Hz, 4H), 7.42 (d, $J=1.7$ Hz, 8H), 1.31 (s, 72H). $^{13}C\{^1H\}$ NMR ($CDCl_3$, 126 MHz) δ: 151.9, 147.1, 143.3, 138.3, 134.9, 130.9, 130.5, 124.4, 122.8, 121.8, 121.4, 114.4, 113.0, 34.9, 31.4. HR-MS (ESI): m/z $[M]^{2+}$ calcd for $C_{94}H_{107}N_{10}Zn$ 720.3941; found 720.3960.

Zn3: proligand **L3** (0.1 g, 0.18 mmol), $Zn(BF_4)_2 \cdot 3H_2O$ (0.09 mmol), 0.1 g, yield 81%. ^1H NMR (DMSO-d_6, 500 MHz) δ: 9.15 (s, 4H), 8.57 (s, 4H), 8.11 (d, $J=8$ Hz, 4H), 8.01 (t, $J=8$ Hz, 2H), 7.75 (m, 8H), 7.56 (d, $J=7$ Hz, 8H), 7.31 (tt, $J=2.5$, 9.5 Hz, 4H). $^{13}C\{^1H\}$ NMR (DMSO-d_6, 126 MHz) δ: 134.2, 126.1, 125.5, 120.1, 119.7, 117.5, 114.7, 112.4, 110.1, 109.2. $^{19}F\{^1H\}$ NMR (DMSO-d_6, 300 MHz) δ: 148.3. HR-MS (ESI): m/z $[M]^{2+}$ calcd for $C_{62}H_{35}F_8N_{10}Zn$ 567.1060; found 568.1047.

Zn4: proligand **L4** (0.1 g, 0.12 mmol), $Zn(BF_4)_2 \cdot 3H_2O$ (0.12 mmol), obtained 0.09 g, yield 79%.^1H NMR ($CDCl_3$, 500 MHz): δ: 8.73 (s, 4H), 8.39-8.38 (m, 10H), 7.23–7.18 (m, 26H), 7.04–6.97 (m, 34H), 6.29 (d, $J=9$ Hz, 4H). $^{13}C\{^1H\}$ NMR ($CDCl_3$, 126 MHz) δ: 148.4, 147.2, 147.1, 143.1, 138.1, 130.1, 129.6, 129.4, 128.9, 128.3, 127.5, 125.3, 124.9, 123.8, 123.6, 122.9, 121.4, 114.3, 113.2. HR-MS (ESI): m/z $[M]^{2+}$ calcd for $C_{110}H_{79}N_{14}Zn$ 830.2907; found 830.2957.

X-ray diffractometric analysis

The crystals were placed in oil, and a single crystal was selected, mounted on a glass fibre and placed in a low temperature N_2 stream. X-ray diffraction data collection was carried out on a Bruker PHOTON III DUO CPAD diffractometer equipped with an Oxford Cryosystem liquid N_2 device, using Mo–Kα radiation ($\lambda=0.71073$ Å). The crystal-detector distance was 38 mm. The cell parameters were determined (APEX3 software)[58] from reflections taken from 1 set of 180 frames at 1 s exposure. The structure was solved using the program SHELXT-2018.[59] The refinement and all further calculations were carried out using SHELXL-2018.[60] The H-atoms were included in calculated positions and treated as riding atoms using SHELXL default parameters. The non-H atoms were refined anisotropically, using weighted full-matrix least-squares on F^2. A semi-empirical absorption correction was applied using SADABS in APEX3;[58] transmission factors: $T_{min}/T_{max}=0.6357/0.7456$. The residual electron density was assigned to six molecules of the acetone solvent [209 *e* per cell, 6 molecules of C_3H_6O would give 192 *e*]. Deposition Number 2239324 (for **Zn2·CH$_3$COCH$_3$**) https://www.ccdc.cam.ac.uk/services/structures?id=doi:10.1002/cptc.202300092 contains the supplementary crystallographic data for this paper. These data are provided free of charge by the joint Cambridge Crystallographic Data Centre and Fachinformationszentrum Karlsruhe http://www.ccdc.cam.ac.uk/structures Access Structures service.

Photophysical characterization

Instrument details. Absorption spectra were measured on a Varian Cary 100 double-beam UV-VIS spectrophotometer and baseline corrected. Steady-state emission spectra were recorded on a Horiba Jobin-Yvon IBH FL-322 Fluorolog 3 spectrometer equipped with a 450 W xenon arc lamp, double-grating excitation, and emission monochromators (2.1 nm mm^{-1} of dispersion; 1200 grooves mm^{-1}) and a Hamamatsu R13456 red sensitive Peltier-cooled PMT detector. Emission and excitation spectra were corrected for source intensity (lamp and grating) and emission spectral response (detector and grating) by standard correction curves. Time-resolved measurements were performed using the time-correlated single-photon counting (TCSPC) electronics option of the TimeHarp 260 board installed on a PicoQuant FluoTime 300 fluorimeter (PicoQuant GmbH, Germany), equipped with a PDL 820 laser pulse driver. A pulsed laser diode LDH-P-C-375 ($\lambda=375$ nm, pulse full width at half maximum FWHM < 40 ps, repetition rate 200 kHz–40 MHz) was used to excite the sample and mounted directly on the sample chamber at 90°. The photons were collected by a PMA Hybrid-07 single photon counting detector. The data were acquired by using the commercially available software EasyTau II (PicoQuant GmbH, Germany), while data analysis was performed using the built-in software FluoFit (PicoQuant GmbH, Germany).

Methods. For time resolved measurements, data fitting was performed by employing the maximum likelihood estimation (MLE) methods and the quality of the fit was assessed by inspection of the reduced χ^2 function and of the weighted residuals. For multi-exponential decays, the intensity, namely I(*t*), has been assumed to decay as the sum of individual single exponential decays [Equation (5)]:

$$I(t) = \sum_{i=1}^{n} \alpha_i exp\left(-\frac{t}{\tau_i}\right) \quad (5)$$

where τ_i are the decay times and α_i are the amplitude of the component at $t=0$. In the tables, the percentages to the pre-exponential factors, α_i, are listed upon normalization.

Intensity average lifetimes were calculated by using the following equation [Equation (6)]:[61]

$$\bar{\tau} = \frac{a_1\tau_1^2 + a_2\tau_2^2}{a_1\tau_1 + a_2\tau_2} \quad (6)$$

Luminescence quantum yields were measured in optically dilute solutions (optical density < 0.1 at the excitation wavelength). The absolute photoluminescence quantum yields (PLQY) were measured on a Hamamatsu Quantaurus-QY C11347-11 integrating sphere in air-equilibrated condition using an empty quartz tube as the reference upon excitation at $\lambda_{exc} = 320$ nm.

Cyclic voltammetry

Anhydrous N,N-dimethylformamide (DMF) and tetra-n-butylammonium tetrafluoroborate ($TBABF_4$, Sigma-Aldrich, 99%) were used as received. Cyclic voltammetry was performed on a Radiometer PST006 potentiostat using a conventional three electrode cell. The saturated calomel electrode (SCE) was separated from the test compartment using a bridge tube. The solutions of studied complexes (0.9 mM **Zn1** complex; 0.5 mM **Zn4** complex) were purged with argon before each measurement. The test solution was *N*,*N*′-dimethylformamide containing 0.1 M $TBABF_4$ as the supporting electrolyte. The working electrode was a vitreous carbon rod (1 cm^2) wire and the counter-electrode was a Pt wire. After the measurement, ferrocene (Fc) was added as the internal reference for calibration. All potentials were quoted versus SCE. In these conditions, the redox potential of the couple Fc^+/Fc was found at 0.47 V. In all the experiments, the scan rate was 100 mV/s.

Computational details

All calculations have been performed with ADF 2019[62] at DFT level of theory with B3LYP functional.[63] All atoms were described by the TZP basis set.[64] Dispersion corrections were introduced through Grimme's correction[65] and relativistic effects through ZORA Hamiltonian.[66] Solvent corrections (DMF) were taken into account by using the polarizable continuum model (PCM) formalism.[67] Structures were fully optimized and the absorption spectra computed by TD-DFT on the stationary point encountered. Emission wavelength was computed by optimizing the lowest excited singlet states in the same conditions. The nature of the excited states was determined by electron density difference between the ground and the excited state computed with Dgrid package[68] using ADF wavefunction.

Acknowledgements

The Université de Strasbourg and the CNRS are kindly acknowledged for financial support. M.M. gratefully acknowledges the French Agence Nationale de Recherche (ANR) for funding the grants ANR-18-CE06-007-01 "SoftAction", ANR-20-CE29-0021 "PhotoMecha" and ANR-21-CE29-0015 "ChirON". C.G. thanks the computing center of the Université de Strasbourg for computing time. V.G. thanks the College Doctoral of the Université de Strasbourg for partially funding his PhD fellowship. Robin Fleischel of the UFR de Mathématique et d'Informatique of the Université de Strasbourg is kindly acknowledged for help with coding and data processing. Electrochemical experiments were carried out on the PhotoNS Platform of the L2CM Laboratory. The authors greatly acknowledge the Plateforme PhotoNS of the L2CM Laboratory, University of Lorraine.

Conflict of Interests

The authors declare no conflict of interest.

Data Availability Statement

The data that support the findings of this study are available from the corresponding author upon reasonable request.

Keywords: charge transfer · density functional calculations · N ligands · photophysics · zinc

[1] E. Vauthey, *ChemPhysChem* **2012**, *13*, 2001–2011.
[2] T. Arlt, S. Schmidt, W. Kaiser, C. Lauterwasser, M. Meyer, H. Scheer, W. Zinth, *Proc. Natl. Acad. Sci. USA* **1993**, *90*, 11757–11761.
[3] W. Holzapfel, U. Finkele, W. Kaiser, D. Oesterhelt, H. Scheer, H. U. Stilz, W. Zinth, *Proc. Natl. Acad. Sci. USA* **1990**, *87*, 5168–5172.
[4] M. H. Vos, F. Rappaport, J.-C. Lambry, J. Breton, J.-L. Martin, *Nature* **1993**, *363*, 320–325.
[5] G. Bottari, O. Trukhina, M. Ince, T. Torres, *Coord. Chem. Rev.* **2012**, *256*, 2453–2477.
[6] A. J. Cowan, J. R. Durrant, *Chem. Soc. Rev.* **2013**, *42*, 2281–2293.
[7] R. S. K. Kishore, O. Kel, N. Banerji, D. Emery, G. Bollot, J. Mareda, A. Gomez-Casado, P. Jonkheijm, J. Huskens, P. Maroni, M. Borkovec, E. Vauthey, N. Sakai, S. Matile, *J. Am. Chem. Soc.* **2009**, *131*, 11106–11116.
[8] Z. R. Grabowski, K. Rotkiewicz, W. Rettig, *Chem. Rev.* **2003**, *103*, 3899–4032.
[9] J. J. Piet, W. Schuddeboom, B. R. Wegewijs, F. C. Grozema, J. M. Warman, *J. Am. Chem. Soc.* **2001**, *123*, 5337–5347.
[10] M. Zander, W. Rettig, *Chem. Phys. Lett.* **1984**, *110*, 602–610.
[11] R. Stahl, C. Lambert, C. Kaiser, R. Wortmann, R. Jakober, *Chem. Eur. J.* **2006**, *12*, 2358–2370.
[12] C. Sissa, A. Painelli, M. Blanchard-Desce, F. Terenziani, *J. Phys. Chem. B* **2011**, *115*, 7009–7020.
[13] C. Trinh, K. Kirlikovali, S. Das, M. E. Ener, H. B. Gray, P. Djurovich, S. E. Bradforth, M. E. Thompson, *J. Phys. Chem. C* **2014**, *118*, 21834–21845.
[14] M. Kellogg, A. Akil, D. S. Muthiah Ravinson, L. Estergreen, S. E. Bradforth, M. E. Thompson, *Faraday Discuss.* **2019**, *216*, 379–394.
[15] S. Kusaka, R. Sakamoto, Y. Kitagawa, M. Okumura, H. Nishihara, *Chem. Asian J.* **2012**, *7*, 907–910.
[16] D. H. Oh, S. G. Boxer, *J. Am. Chem. Soc.* **1989**, *111*, 1130–1131.
[17] A. T. Yeh, C. V. Shank, J. K. McCusker, *Science* **2000**, *289*, 935–938.
[18] M.-E. Moret, I. Tavernelli, M. Chergui, U. Rothlisberger, *Chem. Eur. J.* **2010**, *16*, 5889–5894.
[19] R. Sakamoto, T. Iwashima, M. Tsuchiya, R. Toyoda, R. Matsuoka, J. F. Kögel, S. Kusaka, K. Hoshiko, T. Yagi, T. Nagayama, H. Nishihara, *J. Mater. Chem. A* **2015**, *3*, 15357–15371.
[20] D. Tungulin, J. Leier, A. B. Carter, A. K. Powell, R. Q. Albuquerque, A. N. Unterreiner, C. Bizzarri, *Chem. Eur. J.* **2019**, *25*, 3816–3827.
[21] I. B. Lozada, J. D. Braun, J. A. G. Williams, D. E. Herbert, *Inorg. Chem.* **2022**, *61*, 17568–17578.
[22] H. Yersin, *Highly Efficient OLEDs with Phosphorescent Materials*, John Wiley & Sons **2008**.
[23] A. Bonfiglio, M. Mauro, *Eur. J. Inorg. Chem.* **2020**, *2020*, 3427–3442.
[24] A. F. Henwood, E. Zysman-Colman, *Top. Curr. Chem.* **2016**, *374*.
[25] N. Armaroli, H. J. Bolink (Eds.), *Photoluminescent Materials and Electroluminescent Devices*, Springer **2017**.
[26] Y. Chi, T.-K. Chang, P. Ganesan, P. Rajakannu, *Coord. Chem. Rev.* **2017**, *346*, 91–100.
[27] C. Cebrián, M. Mauro, *Beilstein J. Org. Chem.* **2018**, *14*, 1459–1481.
[28] A. F. Henwood, E. Zysman-Colman, *Chem. Commun.* **2017**, *53*, 807–826.
[29] J. Lee, H.-F. Chen, T. Batagoda, C. Coburn, P. I. Djurovich, M. E. Thompson, S. R. Forrest, *Nat. Mater.* **2016**, *15*, 92–98.

[30] M. Elie, F. Sguerra, F. Di Meo, M. D. Weber, R. Marion, A. Grimault, J.-F. Lohier, A. Stallivieri, A. Brosseau, R. B. Pansu, J.-L. Renaud, M. Linares, M. Hamel, R. D. Costa, S. Gaillard, *ACS Appl. Mater. Interfaces* **2016**, *8*, 14678–14691.
[31] M. D. Weber, E. Fresta, M. Elie, M. E. Miehlich, J.-L. Renaud, K. Meyer, S. Gaillard, R. D. Costa, *Adv. Funct. Mater.* **2018**, *28*, 1707423.
[32] S. Shi, M. C. Jung, C. Coburn, A. Tadle, D. Sylvinson M R, P. I. Djurovich, S. R. Forrest, M. E. Thompson, *J. Am. Chem. Soc.* **2019**, *141*, 3576–3588.
[33] R. Hamze, J. L. Peltier, D. Sylvinson, M. Jung, J. Cardenas, R. Haiges, M. Soleilhavoup, R. Jazzar, P. I. Djurovich, G. Bertrand, M. E. Thompson, *Science* **2019**, *363*, 601–606.
[34] M. Gernert, L. Balles-Wolf, F. Kerner, U. Müller, A. Schmiedel, M. Holzapfel, C. M. Marian, J. Pflaum, C. Lambert, A. Steffen, *J. Am. Chem. Soc.* **2020**, *142*, 8897–8909.
[35] M. Wallesch, D. Volz, D. M. Zink, U. Schepers, M. Nieger, T. Baumann, S. Bräse, *Chem. Eur. J.* **2014**, *20*, 6578–6590.
[36] D. Volz, M. Wallesch, C. Fléchon, M. Danz, A. Verma, J. M. Navarro, D. M. Zink, S. Bräse, T. Baumann, *Green Chem.* **2015**, *17*, 1988–2011.
[37] A. Barbieri, G. Accorsi, N. Armaroli, *Chem. Commun.* **2008**, 2185–2193.
[38] R. Czerwieniec, M. J. Leitl, H. H. H. Homeier, H. Yersin, *Coord. Chem. Rev.* **2016**, *325*, 2–28.
[39] A. N. Gusev, M. A. Kiskin, E. V. Braga, M. A. Kryukova, G. V. Baryshnikov, N. N. Karaush-Karmazin, V. A. Minaeva, B. F. Minaev, K. Ivaniuk, P. Stakhira, H. Ågren, W. Linert, *ACS Appl. Electron. Mater.* **2021**, *3*, 3436–3444.
[40] F. Dumur, L. Beouch, M.-A. Tehfe, E. Contal, M. Lepeltier, G. Wantz, B. Graff, F. Goubard, C. R. Mayer, J. Lalevée, D. Gigmes, *Thin Solid Films* **2014**, *564*, 351–360.
[41] Y.-Z. Xie, G.-G. Shan, P. Li, Z.-Y. Zhou, Z.-M. Su, *Dyes Pigm.* **2013**, *96*, 467–474.
[42] G. Cheng, G. K.-M. So, W.-P. To, Y. Chen, C.-C. Kwok, C. Ma, X. Guan, X. Chang, W.-M. Kwok, C.-M. Che, *Chem. Sci.* **2015**, *6*, 4623–4635.
[43] A. Gusev, E. Braga, Y. Baluda, M. Kiskin, M. Kryukova, N. Karaush-Karmazin, G. Baryshnikov, A. Kuklin, B. Minaev, H. Ågren, W. Linert, *Polyhedron* **2020**, *191*, 114768.
[44] D. Temerova, K. S. Kisel, T. Eskelinen, A. S. Melnikov, N. Kinnunen, P. Hirva, J. R. Shakirova, S. P. Tunik, E. V. Grachova, I. O. Koshevoy, *Inorg. Chem. Front.* **2021**, *8*, 2549–2560.
[45] J. Dam, Z. Ismail, T. Kurebwa, N. Gangat, L. Harmse, H. M. Marques, A. Lemmerer, M. L. Bode, C. B. de Koning, *Eur. J. Med. Chem.* **2017**, *126*, 353–368.
[46] G. A. Ardizzoia, G. Colombo, B. Therrien, S. Brenna, *Eur. J. Inorg. Chem.* **2019**, *2019*, 1825–1831.
[47] G. A. Ardizzoia, S. Brenna, S. Durini, B. Therrien, *Polyhedron* **2015**, *90*, 214–220.
[48] G. Volpi, E. Priola, C. Garino, A. Daolio, R. Rabezzana, P. Benzi, A. Giordana, E. Diana, R. Gobetto, *Inorg. Chim. Acta* **2020**, *509*, 119662.
[49] M. Strianese, S. Brenna, G. Attilio Ardizzoia, D. Guarnieri, M. Lamberti, I. D'Auria, C. Pellecchia, *Dalton Trans.* **2021**, *50*, 17075–17085.
[50] Y. Sakai, Y. Sagara, H. Nomura, N. Nakamura, Y. Suzuki, H. Miyazaki, C. Adachi, *Chem. Commun.* **2015**, *51*, 3181–3184.
[51] A. Steinegger, S. M. Borisov, *ACS Omega* **2020**, *5*, 7729–7737.
[52] J. Xiong, K. Li, T. Teng, X. Chang, Y. Wei, C. Wu, C. Yang, *Chem. Eur. J.* **2020**, *26*, 6887–6893.
[53] E. Jouaiti, V. Giuso, D. Cianfarani, N. Kyritsakas, C. Gourlaouen, M. Mauro, *Chem. Asian J.* **2022**, *17*, e202200903.
[54] N. Mataga, Y. Kaifu, M. Koizumi, *Bull. Chem. Soc. Jpn.* **1955**, *28*, 690–691.
[55] E. Lippert, *Z. Naturforsch. A* **1955**, *10*, 541–545.
[56] M. R. Pinto, Y. Takahata, T. D. Z. Atvars, *J. Photochem. Photobiol. A* **2001**, *143*, 119–127.
[57] A. Weller, *Zeitschrift für Phys. Chemie* **1982**, *133*, 93–98.
[58] M86-EXX229 V1 APEX3 User Manual, Bruker AXS Inc., Madison, USA **2016**.
[59] G. M. Sheldrick, *Acta Crystallogr. Sect. A* **2015**, *71*, 3–8.
[60] G. M. Sheldrick, *Acta Crystallogr. Sect. C* **2015**, *71*, 3–8.
[61] J. R. Lakowicz, *Principles of Fluorescence Spectroscopy*, Springer **2006**.
[62] ADF 2019, SCM, Theoretical Chemistry, Vrije Universiteit, Amsterdam, The Netherlands, http://www.scm.com.
[63] P. J. Stephens, F. J. Devlin, C. F. Chabalowski, M. J. Frisch, *J. Phys. Chem.* **1994**, *98*, 11623–11627.
[64] E. Van Lenthe, E. J. Baerends, *J. Comput. Chem.* **2003**, *24*, 1142–1156.
[65] S. Grimme, J. Antony, S. Ehrlich, H. Krieg, *J. Chem. Phys.* **2010**, *132*, 154104.
[66] E. van Lenthe, A. Ehlers, E.-J. Baerends, *J. Chem. Phys.* **1999**, *110*, 8943–8953.
[67] C. C. Pye, T. Ziegler, *Theor. Chim. Acta* **1999**, *101*, 396–408.
[68] M. Kohout, DGrid, version 4.6, Radebeul **2011**.

Manuscript received: May 8, 2023
Revised manuscript received: May 19, 2023
Accepted manuscript online: May 22, 2023
Version of record online: June 12, 2023